Published OnlineFirst March 15, 2018; DOI: 10.1158/1541-7786.MCR-17-0665

Metabolism

Molecular Cancer Research

Cholesterol Esterification Inhibition Suppresses Prostate Cancer Metastasis by Impairing the Wnt/β-catenin Pathway

Hyeon Jeong Lee[1,2,3], Jie Li[4], Renee E. Vickman[1,2], Junjie Li[3], Rui Liu[3], Abigail C. Durkes[2], Bennett D. Elzey[2,5], Shuhua Yue[6,7], Xiaoqi Liu[1,4,5], Timothy L. Ratliff[1,2,5], and Ji-Xin Cheng[1,3,5,8]

Abstract

Dysregulation of cholesterol is a common characteristic of human cancers including prostate cancer. This study observed an aberrant accumulation of cholesteryl ester in metastatic lesions using Raman spectroscopic analysis of lipid droplets in human prostate cancer patient tissues. Inhibition of cholesterol esterification in prostate cancer cells significantly suppresses the development and growth of metastatic cancer lesions in both orthotopic and intracardiac injection mouse models. Gene expression profiling reveals that cholesteryl ester depletion suppresses the metastatic potential through upregulation of multiple regulators that negatively impact metastasis. In addition, Wnt/β-catenin, a vital pathway for metastasis, is downregulated upon cholesteryl ester depletion. Mechanistically, inhibition of cholesterol esterification significantly blocks secretion of Wnt3a through reduction of monounsaturated fatty acid levels, which limits Wnt3a acylation. These results collectively validate cholesterol esterification as a novel metabolic target for treating metastatic prostate cancer. *Mol Cancer Res; 16(6); 974–85. ©2018 AACR.*

Introduction

Cholesterol is an essential component of mammalian cells and is tightly regulated at multiple levels (1, 2). Cells obtain cholesterol from either *de novo* synthesis or uptake of low-density lipoprotein (LDL) for construction of membrane structures, steroidogenesis, or modulation of protein trafficking and activity (2, 3). Cholesterol overloading causes cytotoxicity, and for most cell types, cholesterol efflux is essential for maintaining its homeostasis (4). Another mechanism for avoiding free cholesterol toxicity is by storing excess cholesterol into lipid droplets. This process involves conversion of cholesterol into cholesteryl ester (CE) by acyl-coenzyme A: cholesterol acyltransferase (ACAT; refs. 1, 5). Cholesterol homeostasis is maintained through a feedback-regulated manner (6) and disruption of this balance is associated with many diseases such as atherosclerosis, metabolic diseases, and cancers. Analysis of The Cancer Genome Atlas (TCGA) database demonstrates correlation between cholesterol level and cancer patient survival (7), which supports an important role of abnormal cholesterol metabolism in cancer development. Other studies on mechanisms have also shown the connection between oncogenic pathway and altered cholesterol metabolism during cancer progression (8, 9). It was observed several decades ago that cholesterol accumulates in prostate cancer (10). Since then, an increasing number of studies support the indispensable roles of cholesterol in prostate cancer progression (11). One hypothesis is that the accumulated cholesterol from either *de novo* synthesis or uptake in prostate cancer provides precursor for androgen synthesis within tumor for the development of castration-resistant prostate cancer (12, 13). Another hypothesis is that increased cholesterol level supports prostate cancer growth by providing key membrane components such as lipid rafts (14, 15). Other studies have shown that a certain signaling molecule (16) and cell-cycle regulator (17) are sensitive to intracellular cholesterol level. In the meanwhile, suppression of cholesterol efflux pathway in advanced prostate cancer was observed (18), which further supports increased cholesterol level during prostate cancer progression. These extensive studies on functional roles of cholesterol accumulation in prostate cancer regulated by synthesis, uptake, and efflux have provided important insights. However, our understanding of cholesterol homeostasis in prostate cancer is incomplete, as another critical aspect of cholesterol metabolism, cholesterol esterification, is relatively understudied. Being an important buffering mechanism for detoxifying excess free cholesterol (2), esterification of cholesterol may be necessary for prostate cancer cells to cope with high intracellular cholesterol level.

We previously showed an aberrant accumulation of CE in lipid droplets inside cancerous lesions by implementing label-free Raman spectroscopic imaging of lipid droplets in human prostate cancer tissues (19). This accumulation was found to be a result of

[1]Interdisciplinary Life Science Program, Purdue University, West Lafayette, Indiana. [2]Department of Comparative Pathobiology, Purdue University, West Lafayette, Indiana. [3]Weldon School of Biomedical Engineering, Purdue University, West Lafayette, Indiana. [4]Department of Biochemistry, Purdue University, West Lafayette, Indiana. [5]Center for Cancer Research, Purdue University, West Lafayette, Indiana. [6]School of Biological Science and Medical Engineering, Beihang University, Beijing, China. [7]Beijing Advanced Innovation Center for Biomedical Engineering, Beihang University, Beijing, China. [8]Department of Biomedical Engineering, Department of Electrical and Computer Engineering, Photonics Center, Boston University, Boston, Massachusetts.

Note: Supplementary data for this article are available at Molecular Cancer Research Online (http://mcr.aacrjournals.org/).

Corresponding Author: Ji-Xin Cheng, Boston University, 8 St. Mary's St, Boston, MA 02215. Phone: 617-353-1276; Fax: 617-353-1276; E-mail: jxcheng@bu.edu

doi: 10.1158/1541-7786.MCR-17-0665

Published OnlineFirst March 15, 2018; DOI: 10.1158/1541-7786.MCR-17-0665

loss of tumor suppressor PTEN and subsequent activation of PI3K/Akt pathway. Increased LDL uptake is the major source of such accumulation. Depleting CE by ACAT inhibition reduces prostate cancer proliferation and growth in a mouse xenograft model (19). This study serves as a foundation for developing a therapeutic approach using ACAT as a target. Nevertheless, it remains unclear what kind of role CE accumulation plays in prostate cancer metastasis and whether metastasis can be suppressed through CE depletion. Notably, early-stage prostate cancer is often treated successfully, but late-stage prostate cancer, where cancers have been spread to distant lymph nodes, bones, or other organs, has a five-year survival rate as low as 29% (20), making metastasis the major cause of prostate cancer mortality in men. Given that there is currently no effective treatment for this disease (21), a deeper understanding into the role of cholesterol esterification in prostate cancer metastasis would be valuable to the development of novel treatment approaches for metastatic prostate cancer.

In this study, we reveal that CE accumulation is a metabolic signature of human metastatic prostate cancer. We further demonstrate the suppression of both development and growth of metastatic prostate cancer by inhibiting cholesterol esterification in an orthotopic mouse model and an intracardiac injection model. Through gene expression profiling, we identified downregulation of Wnt/β-catenin pathway after CE depletion, confirmed by β-catenin protein levels and distribution in prostate cancer cells. We further show evidence supporting that CE depletion lowers fatty acid availability for Wnt3a acylation, which is essential for Wnt-mediated cell migration. These results collectively support that inhibiting cholesterol esterification suppresses prostate cancer metastasis through impairing Wnt/β-catenin signaling, which opens a new opportunity for treating metastatic prostate cancer.

Materials and Methods

Human metastatic prostate cancer tissue specimens and cell lines

The studies were conducted in accordance with Declaration of Helsinki. The study of human patient specimens was approved by the institutional review board at Purdue University (West Lafayette, IN). Deidentified frozen specimens of human metastatic prostate cancer tissues were purchased from Johns Hopkins Hospital (Baltimore, MD). Stimulated Raman scattering (SRS) imaging and confocal Raman spectroscopy was performed on these tissue slices (~20 μm) without any processing or labeling.

Authenticated PC-3, LNCaP, and DU145 were obtained from ATCC more than 6 months ago. PC-3M cell line was obtained and authenticated from M.D. Anderson Cancer Center Characterized Cell Line Core in 2017. Additional cell line authentication and mycoplasma testing have not been tested by authors after purchase. RPMI 1640, F-12K, and nonessential amino acids (NEAA) were purchased from Life Technologies. Eagle minimum essential medium (EMEM) was purchased from ATCC. FBS was purchased from Atlanta Biologicals. Cells were cultured in the following media: PC-3M in RPMI1640 supplemented with 10% FBS and 0.1 mmol/L NEAA, PC-3 in F-12K supplemented with 10% FBS, LNCaP-HP was derived upon continuous passage from original LNCaP (ATCC) in RPMI1640 supplemented with 10% FBS until the passage number was over 81 following the procedure reported (22, 23), DU145 PTEN-KD cell line in EMEM supplemented with 10% FBS and 5 μg/mL puromycin (Life Technologies). All cells were cultured at 37°C in a humidified incubator with 5% CO_2 supply. The passage numbers of all cell lines were below 30 between thawing and use in the experiments.

SRS imaging and quantification of CE in tissues and cultured cells

SRS imaging was performed on a femtosecond SRS microscope, with the laser beating frequency tuned to the C-H stretching vibration band at 2,845 cm^{-1}, as described previously (24). No cell or tissue damage was observed during the imaging procedure. Lipid droplet amount was quantified using ImageJ. Specifically, "Threshold" function was used to select lipid droplets in the cells due to their significantly higher signal intensities compared to other cellular structures. "Analyze Particles" function was then used to quantify the area fractions of lipid droplets in the whole image area, then normalized to the cell number counted from the same image. Each image contained approximately 10 cells and represented as $n = 1$.

Confocal Raman was performed as described previously (25). CE percentage in lipid droplets was linearly correlated with the height ratio of the 702 cm^{-1} peak (I_{702}) to the 1,442 cm^{-1} peak (I_{1442}) and expressed as $I_{702}/I_{1442} = 0.00334 \times$ CE percentage (%). CE percentage for each group was obtained by averaging the CE percentage of lipid droplets in 3 to 6 cells as Raman profiles of lipid droplets in the same specimen were nearly the same.

Chemicals and reagents

Avasimin was prepared following the protocol described previously (26). Avasimibe, DMSO, human albumin, cholesteryl oleate, glyceryl trioleate, myristoleic acid, palmitic acid, palmitoleic acid, stearate, oleate, linoleic acid, arachidonic acid, and docosahexaenoic acid were purchased from Sigma-Aldrich. IWP-2 was purchased from Abcam. Recombinant human Wnt3a was purchased from Bio-Techne Corporation. Luciferin was purchased from Perkin Elmer.

Prostate cancer orthotopic mouse model

Orthotopic model was used to study whether avasimin treatment can suppress the development of metastasis in a mouse model. All animal procedures were approved by the Purdue Animal Care and Use Committee. PC-3M cells were injected into the prostate of male, 6-week-old NSG mice (Purdue University Center for Cancer Research via MTA with The Jackson Laboratory) following the protocols reported previously (27, 28). Specifically, 2×10^5 PC-3M cells were mixed with an equal volume of Matrigel HC (Corning) and injected into the prostate gland of the mouse. Ten days after the surgery, mice were randomly assigned into 2 groups for the treatment. Avasimin was dissolved in sterile PBS and administrated daily via intraperitoneal injections at the dose of 75 mg/kg. The dosage for the treatment was selected on the basis of previous animal studies (26). Sterile PBS was used for vehicle group. Primary tumor volume was assessed twice a week with palpation. Body weight was also measured twice a week. After treatment for 25 days, tumors and lung were harvested and prepared for tumor volume measurement, hematoxylin and eosin (H&E) and immunofluorescence chemistry (IFC) staining.

Prostate cancer intracardiac injection mouse model

Intracardiac injection model was used to study the therapeutic effect of avasmin to metastasis already developed in mice by

Published OnlineFirst March 15, 2018; DOI: 10.1158/1541-7786.MCR-17-0665

introducing tumor cells directly into the systemic circulation. All animal procedures were approved by the Purdue Animal Care and Use Committee. PC-3 cells with stable expression of luciferase (PC-3-Luc) were injected into the heart of male, 7-week-old nude mice (Envigo) following the protocols reported previously (27). Specifically, 2×10^5 PC-3-Luc cells were injected into the left ventricle. 7 days after the injection, mice were randomly assigned into 2 groups for the treatment. Avasimin was dissolved in sterile PBS and administrated daily via intraperitoneal injections at the dose of 75 mg/kg. Sterile PBS was used for vehicle group. Tumor growth was monitored every two weeks by bioluminescent imaging using IVIS in Bindley Bioscience Center at Purdue. After treatment for 5 weeks, metastatic lesions in the heart, lungs, pancreas, liver, spleen, intestine, and kidneys were visualized using IVIS. Metastatic lesions were harvested and prepared for H&E and spectroscopic imaging. Histologic examination was performed by a pathologist after H&E staining to confirm metastatic lesions.

Histology and IFC staining

Primary prostate tumor and tissues containing metastatic lesions were fixed in 10% neutral buffered formalin. After paraffin embedding, tissue sections were stained using H&E staining. The adjacent tissue sections were used for IFC staining. After deparaffinization and rehydration of tissue slides, antigens were retrieved using unmasking solution (Vector Laboratories) with a 2100-Retriever (PickCell Laboratories). Tissue slides were then incubated with anti-human mitochondria antibody (Millipore MAB1273, 1:100), anti-Ki-67 antibody (Leica KI67-MM1-L-CE, 1:200), or subjected to TUNEL assay (Roche, 11684817910).

RT-PCR profiler array

Total RNA was extracted from PC-3 treated with DMSO or avasimibe using E.Z.N.A. Total RNA Kit I (Omega Bio-Tek Inc) and reverse transcribed using RT^2 First Strand Kit (Qiagen Inc) following the manufacturer's instructions. The human prostate cancer RT^2 Profiler PCR Array (PAHS-135Z) was purchased from Qiagen Inc and quantitative PCR was conducted following the manufacturer's instructions using Roche LightCycler 96. Data analysis was performed on the basis of the $\Delta\Delta C_t$ method with normalization of the raw data to the housekeeping genes using PCR Array Data Analysis Web portal provided by the manufacturer. To determine fold change in gene expression, the normalized expression of each gene in the avasimibe-treated sample is divided by the normalized expression of the same gene in the control sample. Genes were grouped on the basis of their functions.

Immunoblotting analysis and immunoprecipitation of Wnt3a from medium

Cells were lysed in TBSN buffer (20 mmol/L Tris, pH 8.0, 150 mmol/L NaCl, 0.5% Nonidet P-40, 5 mmol/L EGTA, 1.5 mmol/L EDTA, 0.5 mmol/L Na_3VO_4, 20 mmol/L *p*-nitrophenyl phosphate) or RIPA buffer (Sigma-Aldrich) after indicated treatments. Proteins were detected by immunoblotting with the antibodies against active β-catenin (Millipore 05-665, 1:1,000), β-catenin (Cell Signaling Technology 9562S, 1:2,000), Wnt3a (Abcam ab28472, 1:1,000), and β-actin (Sigma A5441, 1:5,000). The immunoblots were quantified using Image Lab software (Bio-Rad), using β-actin as a loading control.

For immunoprecipitation, 1-mL medium was collected from DU145 PTEN-KD cells and preincubated with 100 μL protein A/G agarose beads (Santa Cruz Biotechnology) on a rotator for overnight at 4°C. The beads were discarded and the supernatant was incubated with anti-Wnt3a antibody (2 μg/mL) on a rotator for 10–12 hours at 4°C and subsequently immunoprecipitated with protein A/G agarose beads while rotating for 2 hours at 4°C. The beads were washed once with RPMI buffer supplemented with protease inhibitor. The proteins were then collected by resuspension in sample buffer and heated for 10 minutes at 50°C. Supernatants were collected and supplemented with 100 mmol/L dithiothreitol, and the mixture was heated for 5 minutes at 95°C before SDS-PAGE.

Fatty acid extraction and measurement

PC-3 cells were starved to deplete the fatty acid pool, after which serum is supplemented with avasimibe (10 μmol/L, 1 days). Free fatty acids were extracted from the cell pellets following the procedure described. Cell pellets were lysed in 200-μL methanol and acidified with 25 mmol/L HCl. Then the sample was mixed with 1-mL iso-octane, and centrifuged at $3{,}000 \times g$ for 1 minute. The top layer was transferred to new vials and the extraction was repeated once with the bottom layer. The combined iso-octane layers were dried under N_2 flow. For quantitative analysis, each fatty acid at known concentration was used as internal standards. Liquid chromatography/mass spectrometry (LC/MS) analysis of fatty acids was performed following the protocol described previously (29).

Migration assay

Migration assay was performed in Transwell chambers (Corning) with 8-μm pore-sized membranes. Cells were pretreated with indicated treatment for 2 days before transferring to the Transwell chambers. A total of 2×10^5 cells were seeded in the top chamber in serum-free media. The bottom chamber was filled with media containing 20% FBS and 50 ng/mL human EGF (Life Technologies). Cells were then incubated for 20 hours at 37°C to migrate. The transwell membranes were fixed and cells that had not migrated through the chamber were removed with a cotton swab. Migrated cells were stained with propidium iodide (Life Technologies) and visualized by confocal fluorescence microscopy. For quantification, average number of cells in three fields for one migration chamber was considered $n = 1$.

Statistical analysis

Results for the animal studies were shown as mean + SEM. Mann–Whitney *U* test was used for comparisons between vehicle and Avasimin-treated groups as the data do not follow normal distribution. Other results were shown as mean + SD, unless stated otherwise, and Student *t* test was performed for the comparisons. $P < 0.05$ was considered statistically significant.

Results

CE accumulation in human metastatic prostate cancer tissues

To map the lipid distribution and composition in metastatic prostate cancer, human patient tissues from multiple metastatic sites, including abdominal soft tissue, liver, adrenal gland, rib, and lymph nodes, were examined by stimulated Raman scattering (SRS) microscopy. C-H–rich lipids were visualized by tuning the laser beating frequency to be resonant with C-H stretching

Published OnlineFirst March 15, 2018; DOI: 10.1158/1541-7786.MCR-17-0665

vibration. Lipid droplets were observed in metastatic lesions of abdominal soft tissue, liver, adrenal gland, rib, and lymph nodes (Fig. 1A). By analyzing the composition of these lipid droplets with confocal Raman microspectroscopy (25), we found characteristic bands for cholesterol rings at 702 cm^{-1} and for ester bond at 1,742 cm^{-1} in the Raman spectra of these lipid droplets (ref. 30; Fig. 1B). These spectroscopic signatures indicate the presence of CE. For quantitative measurement of CE level in these samples, we constructed the calibration curve for molar percentage of CE in the total lipids based on the Raman spectral measurement of emulsions containing cholesteryl oleate and glyceryl trioleate. The height ratio between 702 cm^{-1} cholesterol band and 1,442 cm^{-1} CH_2 bending band was linearly proportional to the molar percentage of CE in the lipid mixture (Fig. 1C). On the basis of the calibration curve, we estimated that lipid droplets in all metastatic lesions are composed of 60% to 80% CE (Fig. 1D). Our analysis suggests that accumulation of CE is a metabolic marker for metastatic prostate cancer.

CE depletion suppresses prostate cancer migration *in vitro* and metastasis *in vivo*

CE accumulation in metastatic tumor suggests a possible functional role of CE in metastasis. We hypothesized that depleting CE by ACAT inhibitor would reduce metastatic potential of prostate cancer. To test this hypothesis, we first examined the migration capability of PC-3M, a metastatic prostate cancer cell line derived from liver metastasis of PC-3 xenograft (31). We treated cultured PC-3M cells with a potent ACAT inhibitor, avasimibe. To confirm the reduction of CE level after avasimibe treatment, we measured Raman spectra of lipid droplets in PC-3M cells using confocal Raman microscopy. The Raman spectral analysis showed a significant reduction in CE level upon avasimibe treatment (Supplementary Fig. S1A–S1C). To assess migration capability, we performed a transwell assay of PC-3M cells pretreated with avasimibe. Our results indicate that migration capability of PC-3M cells was suppressed significantly (Supplementary Fig. S2A and S2B). These results suggest that CE depletion impairs the migration capability of prostate cancer cells.

To examine whether CE depletion can suppress prostate cancer tumor metastasis, we generated an orthotopic mouse model of prostate cancer using the PC-3M cells (27, 28). The mice bearing an orthotopic PC-3M xenograft were treated with either vehicle or avasimin, a systemically injectable nanoformulation of avasimibe (26). As illustrated in Fig. 2A, mice were treated with avasimin daily via intraperitoneal injection and tumor metastasis was assessed at the end of the study by IFC staining of cancer cells in lung tissue sections. Primary prostate tumor growth was monitored over the treatment period. Avasimin treatment reduced the growth rate of primary tumors

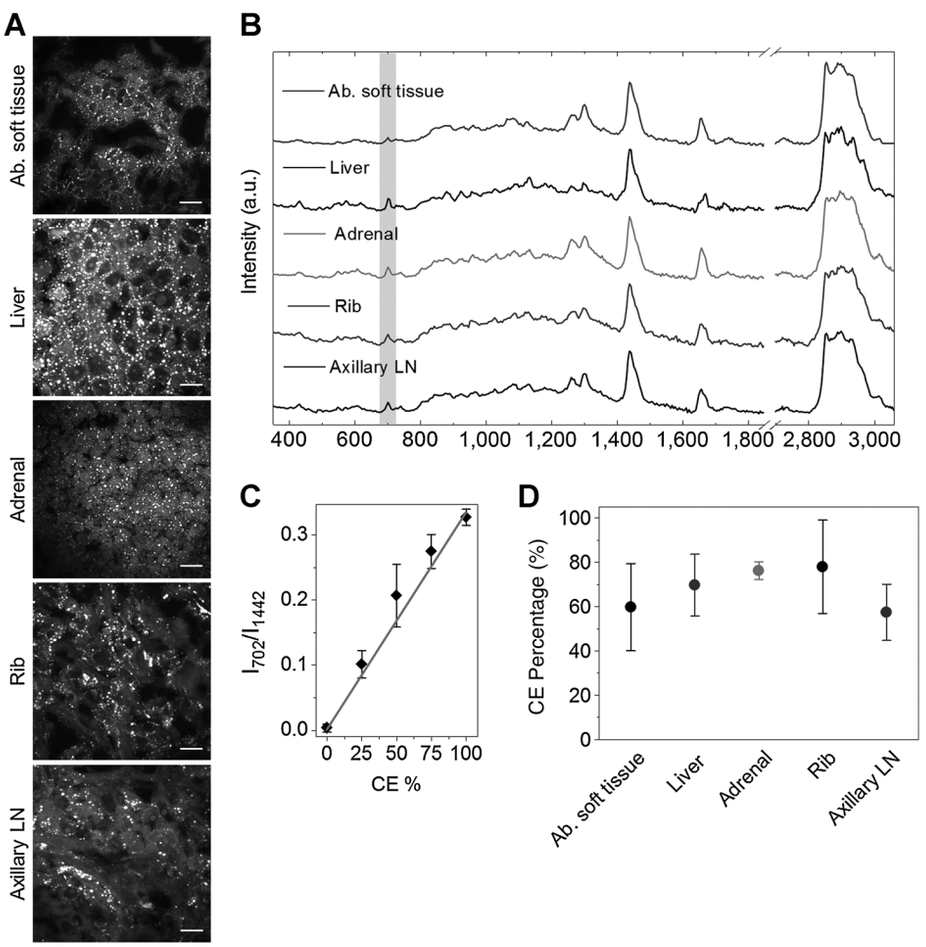

Figure 1.
CE accumulation in human metastatic prostate cancer. **A,** SRS images of metastatic prostate cancer in abdominal soft tissue (ab. soft tissue), liver, adrenal gland, rib, and axillary lymph node (LN). Scale bar, 20 μm. **B,** Raman spectra of lipid droplets in metastatic prostate cancer tissues shown in (**A**). Spectral intensity was normalized by CH_2 bending at 1,442 cm^{-1}. Gray shade indicates the band of cholesterol rings at 702 cm^{-1}. **C,** Calibration curve of molar percentage of CE in total lipid, generated by linear fitting of height ratio between the peak at 702 cm^{-1} (I_{702}) and the peak at 1442 cm^{-1} (I_{1442}). $I_{702}/I_{1442} = 0.00334 \times CE\ \%$. $R^2 = 0.99$. Error bars, SD ($n = 3$). **D,** CE molar percentage in lipid droplets of metastatic prostate cancer in abdominal soft tissue ($n = 3$), liver ($n = 6$), adrenal gland ($n = 3$), rib ($n = 3$), and axillary lymph node ($n = 6$). Error bars, SD.

Published OnlineFirst March 15, 2018; DOI: 10.1158/1541-7786.MCR-17-0665

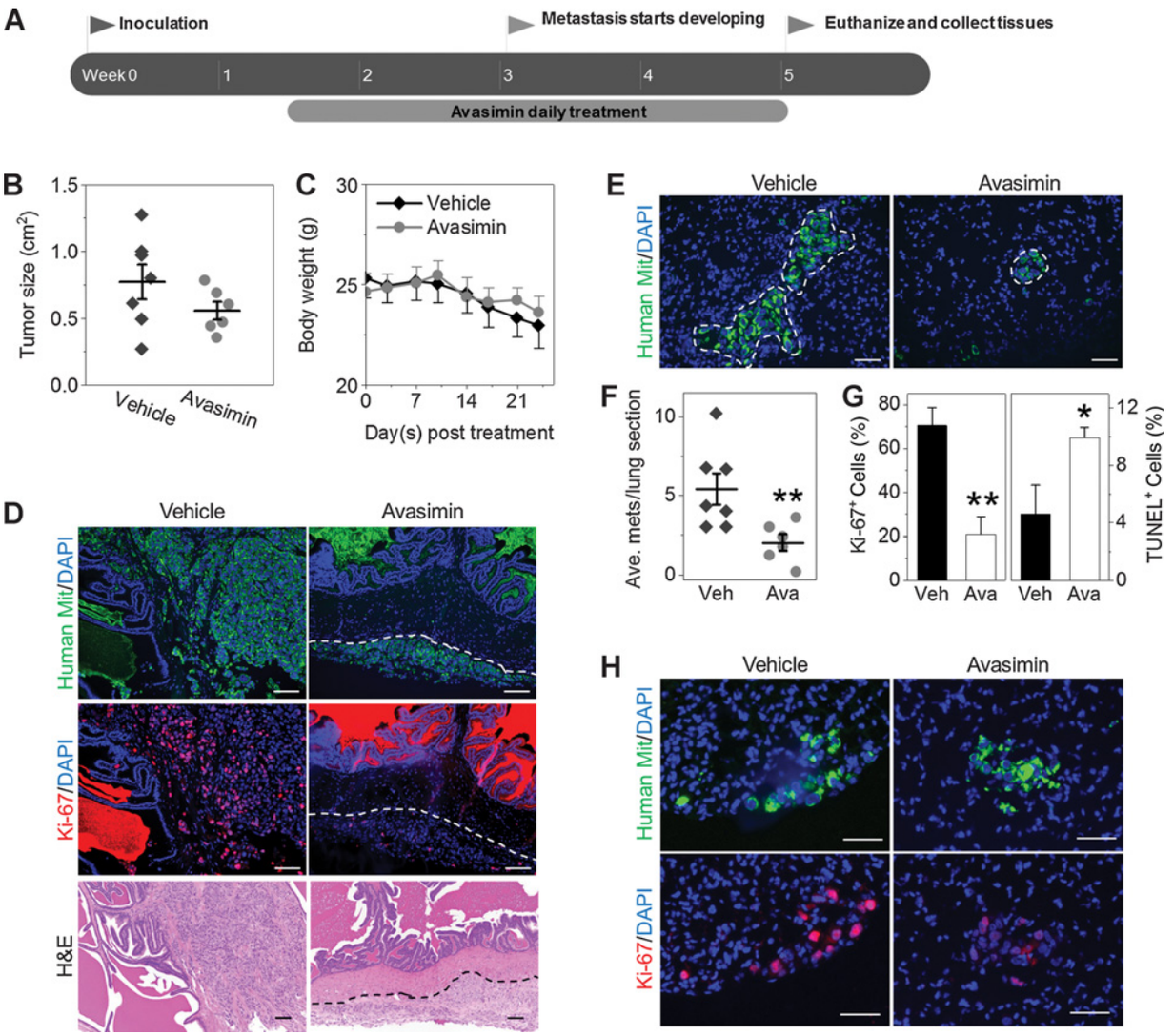

Figure 2.

Prostate cancer metastasis suppressed by targeting cholesterol esterification *in vivo*. **A,** Schematic of prostate cancer orthotopic model study. Avasimin (75 mg/kg) was administrated into mice daily via intraperitoneal injection from 10 days posttransplantation of PC-3M. Vehicle mice were treated with sterile PBS. **B,** Tumor size measured after harvested from vehicle ($n = 7$) and avasimin-treated ($n = 6$) mice. **C,** Body weight of the mice over 25-day treatments. **D,** Representative images of IFC and H&E staining of primary prostate tumor tissues harvested at the end of the study. Dashed lines indicate clear tumor margins in the vehicle group. Scale bar, 100 μm. **E,** Representative images of IFC staining of lung tissues harvested at the end of the study with distinct metastatic clusters indicated. Scale bar, 50 μm. **F,** Quantification of metastatic clusters in lung tissues harvested from vehicle and Avasimin-treated mice. **G,** Percentage of Ki-67–positive (left) and TUNEL-positive (right) cells in metastatic tumor lesions harvested from lung tissues of vehicle and avasimin-treated mice. **H,** Representative images of staining of metastatic tumor lesions in lung tissues harvested from vehicle and avasimin-treated mice. Green, human mitochondria; red, Ki-67; blue, DAPI. Error bars, SEM. *, $P < 0.05$; **, $P < 0.005$.

significantly (Supplementary Fig. S3A) and inhibited the tumor size by approximately 1.4-fold at the end of 25-day treatment (Fig. 2B). No changes in body weight were observed in mice treated with avasimin, indicating no detectable general toxicity to the animals (Fig. 2C). To characterize primary prostate cancers after the treatment, we performed IFC staining of prostate tissues harvested at the end of the study. Anti-human mitochondria antibody was used to specifically label human cancerous cells presented in mouse tissues (Supplementary Fig. S3B). Primary prostate tumors were visualized in tissues from both vehicle and avasimin-treated mice. Importantly, we observed that cancer cells in the vehicle-treated group have invaded into the normal tissues, whereas cancer cells in the avasimin-treated group maintained a confined tumor margin (Fig. 2D). This phenotype was confirmed by pathologic review of the adjacent sections. Furthermore, Ki-67 staining of the adjacent tissue sections showed lower expression of Ki-67 in avasimin-treated group compared with control group, which indicates an anti-proliferating effect of avasimin to the primary tumor (Fig. 2D). Taken together, these results provide evidence that avasimin treatment suppresses invasive phenotype and proliferation of primary prostate cancer.

Published OnlineFirst March 15, 2018; DOI: 10.1158/1541-7786.MCR-17-0665

To assess metastasis in this mouse model, we performed IFC staining of lung tissues with anti-human mitochondria antibody and counted the number of metastatic clusters. Distinct metastasis was defined by a clear cluster of 5 or more cells (ref. 28; Fig. 2E, dashed lines), and counted from the whole lung sections for each mouse. We found a dramatic reduction (~50%) in the number of metastatic clusters in the lung of avasimin-treated mice compared with that in vehicle-treated mice (Fig. 2F), indicating reduced metastatic potential of prostate cancer by avasimin. Moreover, Ki-67 staining of the adjacent tissue sections showed approximately 3.5-fold reduction in the level of Ki-67 in metastatic lesions of avasimin-treated group, indicating antiproliferative activity of avasimin to the metastatic tumors (Fig. 2G and H). TUNEL assay further showed that avasimin increased apoptosis by approximately 1-fold (Fig. 2G). These results collectively support that CE depletion by avasimin suppresses metastatic potential of prostate cancer *in vivo*.

CE depletion directly inhibits growth of metastatic prostate cancer *in vivo*

To determine the clinical potential of CE depletion as a cancer therapy for metastatic prostate cancer, we examined therapeutic efficacy of avasimin in an intracardiac injection model (27), where metastatic prostate cancer cells have already spread to other organs at the start of treatment. Seven days after transplantation of PC-3 cells stably expressing luciferase (PC-3-Luc), the mice were treated with avasimin daily via intraperitoneal injection and tumor growth was monitored biweekly using *in vivo* bioluminescence imaging (Fig. 3A). A significant reduction of tumor growth rate in avasimin-treated group compared with vehicle-treated group was determined (Fig. 3B and C). Body weight measurement showed no significant change during the treatment period, indicating no observable toxicity to the mice (Fig. 3D). After 35 days of avasimin treatment, we observed approximately 4.7-fold reduction in metastatic tumor size in lungs, liver, and spleen/pancreas

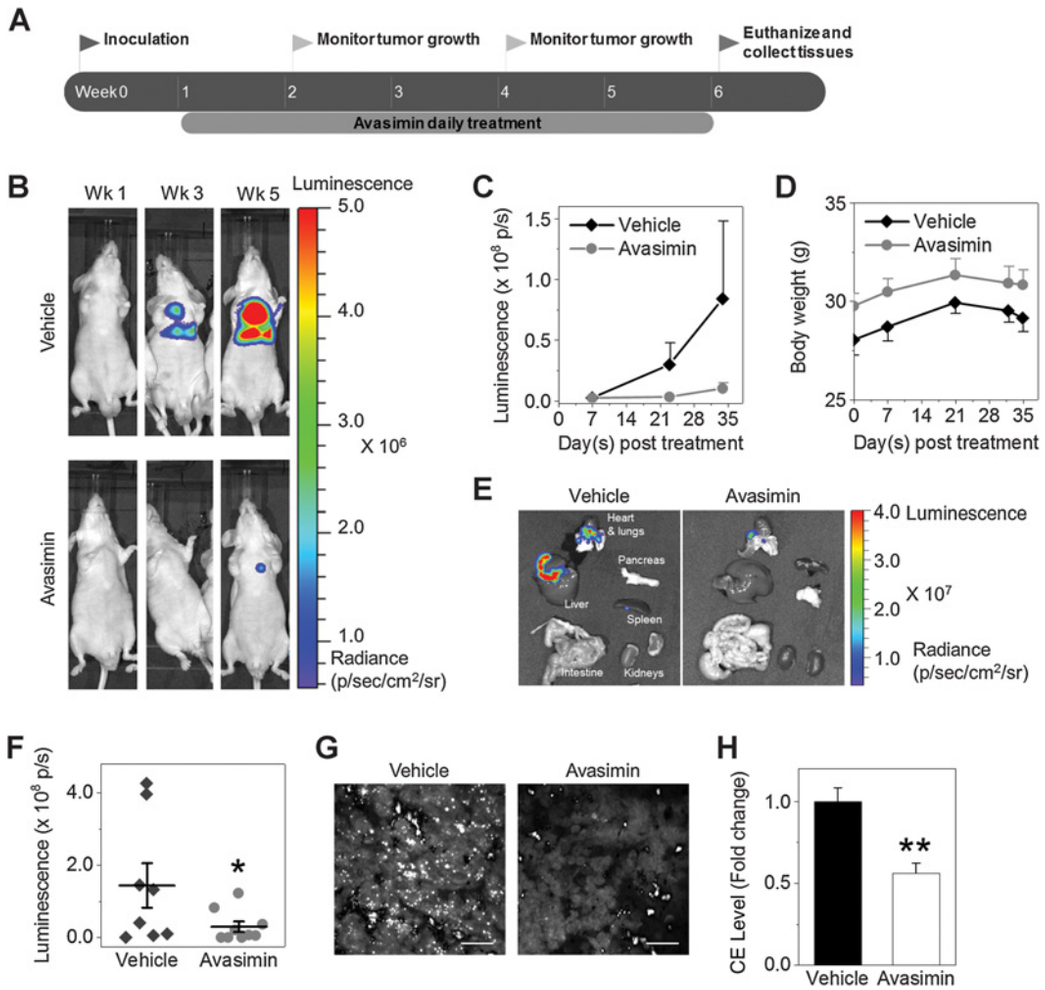

Figure 3.

Metastatic prostate cancer growth inhibited by CE depletion *in vivo*. **A,** Schematic of prostate cancer intracardiac injection model study. Avasimin (75 mg/kg) was administrated into mice daily via intraperitoneal injection from 7 days postinoculation of PC-3-Luc. Vehicle mice were treated with sterile PBS. **B,** Representative IVIS images of mice treated with vehicle ($n = 8$) and avasimin ($n = 9$). **C,** Tumor growth curve quantified by total intensity of IVIS imaging. **D,** Body weight of the mice over 35-day treatments. **E,** Representative IVIS images of metastatic lesions in organs. **F,** Quantification of total intensity of metastatic lesions from IVIS imaging. **G,** SRS images of metastatic lesions in lung tissues harvested at the end of the study. Scale bar, 10 μm. **H,** CE level in the metastatic lesions shown in **G**. Error bars, SEM ($n > 3$). *, $P < 0.05$; **, $P < 0.005$.

Published OnlineFirst March 15, 2018; DOI: 10.1158/1541-7786.MCR-17-0665

(Fig. 3E and F). To evaluate the amount and composition of lipid droplets in the metastatic cancer, we conducted spectroscopic analysis on the frozen lung tissue sections. By SRS imaging of the cancerous lesions, we observed a significant reduction of lipid droplets in avasimin-treated group compared with the control group (Fig. 3G). Confocal Raman spectroscopy further demonstrated that CE level is significantly reduced in these lipid droplets in avasimin-treated group (Fig. 3H), confirming CE depletion after the treatment. Collectively, these results support our hypothesis that depleting CE suppresses metastatic tumor growth.

Gene expression profiling reveals inactivation of Wnt/β-catenin pathway by CE depletion

To unveil the signaling pathways that are associated with CE accumulation and/or depletion, we measured the expression levels of 84 human prostate cancer -related genes after inhibiting cholesterol esterification in PC-3 cells, a metastatic prostate cancer cell line. After confirming CE depletion with avasimibe using confocal Raman microscopy (Fig. 4A and B), the gene expression analysis was performed using a RT-PCR profiler array. The analysis revealed increased expression of regulators that negatively impact metastasis [*DKK3* (32), *DLC1* (33), *FOXO1* (34), *GNRH1*] and genes that are lost in metastatic prostate cancer [*EGR3* (35), *GPX3* (36), *NKX3-1* (37); Fig. 4C; Supplementary Fig. S4A]. At the same time, expression level of proliferating marker gene *MKI67* was decreased dramatically, supporting suppressed cancer proliferation by avasimibe (Fig. 4C; Supplementary Fig. S4B). We also note that CE depletion by avasimibe inhibited expression of *ERG* by approximately 2.8-fold, which is a common proto-oncogene in prostate cancer (Fig. 4C; Supplementary Fig. S4B). Overall, these results indicate that CE depletion by avasimibe suppresses proliferation and metastatic potential of prostate cancer through upregulating multiple negative regulators of metastasis.

Among these metastasis-related genes, *DKK3* is a negative regulator of Wnt/β-catenin pathway, one of the major oncogenic pathways associated with prostate cancer progression and metastasis (38). To confirm that CE depletion inactivates Wnt/β-catenin, immunoblotting of β-catenin was performed in PC-3 cells after ACAT inhibition by avasimibe. Protein level of active β-catenin significantly decreased after avasimibe treatment (Fig. 4D). To eliminate the possibility of nonspecific targeting by ACAT inhibitor, we knocked down ACAT-1 using shRNA (Supplementary Fig. S5A). ACAT-1 knockdown in PC-3 depleted CE (Supplementary Fig. S5B and S5C) and resulted in significant reduction of active β-catenin protein level (Fig. 4D). As active β-catenin translocates to nucleus to act as a transcription factor, we analyzed localization of β-catenin by immunofluorescence staining. CE depletion by either avasimibe or ACAT-1 knockdown reduced nuclear localized β-catenin in PC-3 (Fig. 4E and F; Supplementary Fig. S5D and S5E). To test whether β-catenin inactivation by ACAT inhibition occurs to other aggressive prostate cancer cell lines, we used two other CE-rich aggressive prostate cancer cell models developed from LNCaP and DU145. LNCaP-HP (high passage) is a cell line derived upon continuous passage from LNCaP-LP (low passage) until the passage number exceeds 81 (22), which shows more aggressive and invasive phenotypes compared with LNCaP-LP (22, 23). DU145 with stable PTEN knockdown (DU145 PTEN-KD) is an invasive cell line (39) containing significantly higher CE compared with PTEN wild-type DU145 (19). In both cell models, CE depletion by avasimibe significantly downregulated β-catenin (Supplementary Fig. S6), which also supports inactivation of Wnt/β-catenin signaling by ACAT inhibition. These results collectively indicate that CE depletion inactivates Wnt/β-catenin pathway in aggressive prostate cancer cells.

CE depletion suppresses lipogenic potential of prostate cancer

In Wnt/β-catenin signaling pathway, lipid modification of Wnt is a prerequisite for Wnt activation (40, 41). During the acylation process, fatty acids serve as substrates for this reaction. Interestingly, we observed decreased amount of lipid droplet in avasimin-treated metastatic prostate cancer tissues (Fig. 3G) and avasimibe-treated prostate cancer cells (Fig. 4A), suggesting the possibility of reduced lipogenic potential. Considering the crosstalk between regulation of cholesterol and fatty acid metabolisms, we hypothesized that CE depletion limits availability of fatty acid substrates for Wnt acylation. To test our hypothesis, we performed SRS imaging on lipid droplets in prostate cancer cell lines after ACAT inhibition (Fig. 5A). From analysis of lipid droplet amount in SRS images, we found approximately 1.7-fold reduction in the number of lipid droplets in cells treated with avasimibe or with ACAT-1 shRNA (Fig. 5B). To confirm that such reduction is a result of decreased lipogenesis or uptake, the levels of free fatty acids in prostate cancer were analyzed using LC/MS. Overall, fatty acid synthesis or uptake in CE-depleted cells was reduced for most of fatty acid species tested, except for docosahexaenoic acid (C22:6; Fig. 5C–E). The most significant reduction was found in monounsaturated fatty acids (C14:1, C16:1, C18:1; Fig. 5D). These results support our hypothesis that CE depletion reduces free fatty acid availability in prostate cancer.

CE depletion suppresses cell migration through inhibiting Wnt3a secretion

Stabilization and nuclear transport of β-catenin is a result of Wnt activation, which requires secretion and binding of lipid-modified Wnt to membrane proteins (40, 41). As fatty acid levels in cells decrease, substrates for Wnt acylation become limited. We note that one decreased monounsaturated fatty acid after ACAT inhibition, palmitoleic acid (C16:1), is the fatty acid species used for Wnt acylation required for secretion (41). Therefore, it is likely that Wnt secretion is inhibited as a consequence of CE depletion. First, we tested whether Wnt is inactivated after CE depletion by visualizing its location. By immunofluorescent staining of Wnt3a in prostate cancer cells after avasimibe treatment, we observed membrane localized Wnt3a in control cells (Fig. 6A), indicating activation of Wnt3a. In contrast, avasimibe-treated cells show dramatic approximately 6-fold reduction in membrane-bound Wnt3a, accompanied by intracellular aggregates of Wnt3a (Fig. 6A and B). To eliminate the potential off-target effects of avasimibe, we depleted CE by ACAT-1 knockdown using shRNA. Prostate cancer cells with ACAT-1 knockdown also show approximately 6-fold reduction in membrane-bound Wnt3a compared with control cells (Supplementary Fig. S7A and S7B), confirming the inactivation of Wnt3a after CE depletion. The Wnt3a distribution after avasimibe treatment resembles the localization of Wnt3a after IWP-2 treatment, a potent inhibitor of Wnt3a acylation (Fig. 6A). To further confirm inactivation of Wnt3a, we measured intracellular and secreted Wnt3a after avasimibe treatment using immunoblotting analysis. Intracellular Wnt3a level increased after avasimibe treatment, while medium Wnt3a level decreased by approximately 1.4-fold (Fig. 6C). These results indicate that

Published OnlineFirst March 15, 2018; DOI: 10.1158/1541-7786.MCR-17-0665

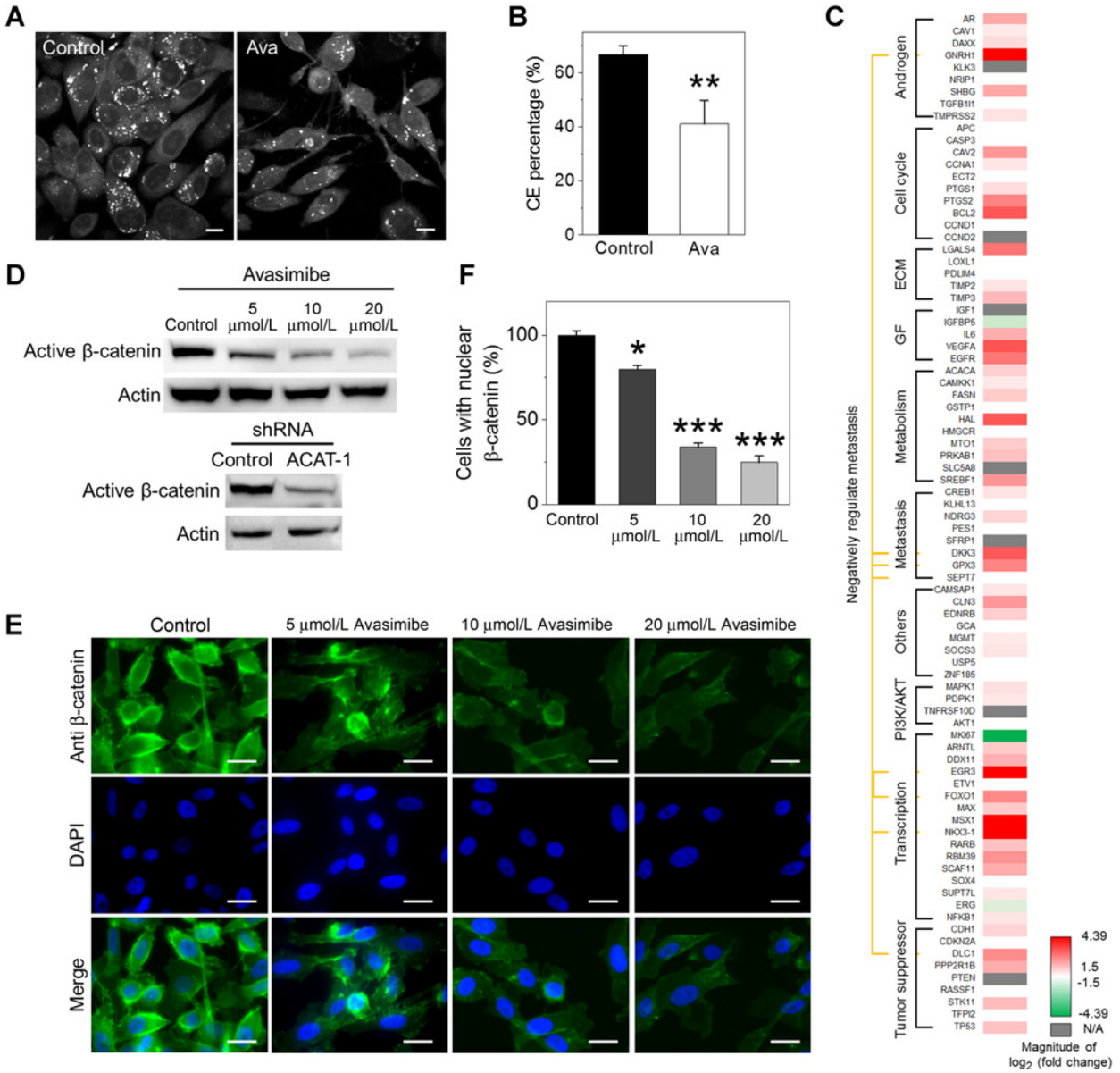

Figure 4.

Depleting CE downregulates Wnt/β-catenin pathway. **A,** SRS images of PC-3 cells treated with avasimibe (5 μmol/L, 3 days). Scale bar, 10 μm. **B,** CE percentage in PC-3 cells shown in **A**. Error bars, SD ($n = 10$). **C,** Expression profiling of 84 prostate cancer -related genes in PC-3 cells shown in (**A**). Upregulation is indicated by shades of red, and downregulation is indicated by shades of green. Gray indicate genes that are not expressed. ± 1.5-fold change is set as a threshold. ECM, extracellular matrix; GF, growth factor. **D,** Immunoblot of antibodies against active β-catenin (dephosphorylated at Ser37 and Thr41) and β-actin in PC-3 cells treated with concentrations of avasimibe as indicated for 2 days or with ACAT-1 shRNA. **E,** Immunofluorescent staining of β-catenin in PC-3 cells treated with concentrations of avasimibe as indicated for 2 days. Scale bar, 10 μm. **F,** Quantification of cells with nuclear β-catenin after avasimibe treatment. Error bars represent SD ($n > 90$ in each group). **, $P < 0.005$; ***, $P < 0.0005$.

avasimibe treatment inactivates Wnt/β-catenin pathway through reducing Wnt secretion.

To test whether Wnt/β-catenin is an essential pathway that links CE accumulation to aggressiveness of prostate cancer, we performed a migration rescue experiment with Wnt3a. CE depletion by avasimibe significantly suppressed migration capability of prostate cancer by approximately 42% (Fig. 6D and E). When Wnt3a was supplemented into the medium, migration capability of the cells was rescued significantly (Fig. 6D and E), although not to the full extent (~86% recovery). These results indicate that CE depletion suppresses prostate cancer aggressiveness largely through Wnt/β-catenin pathway.

On the basis of our data, we propose that blocking cholesterol esterification creates imbalance in cancer lipid metabolism that is important for modulating the activities of Wnt/β-catenin pathway (Fig. 6F). Under normal condition, excess cholesterol in prostate

Published OnlineFirst March 15, 2018; DOI: 10.1158/1541-7786.MCR-17-0665

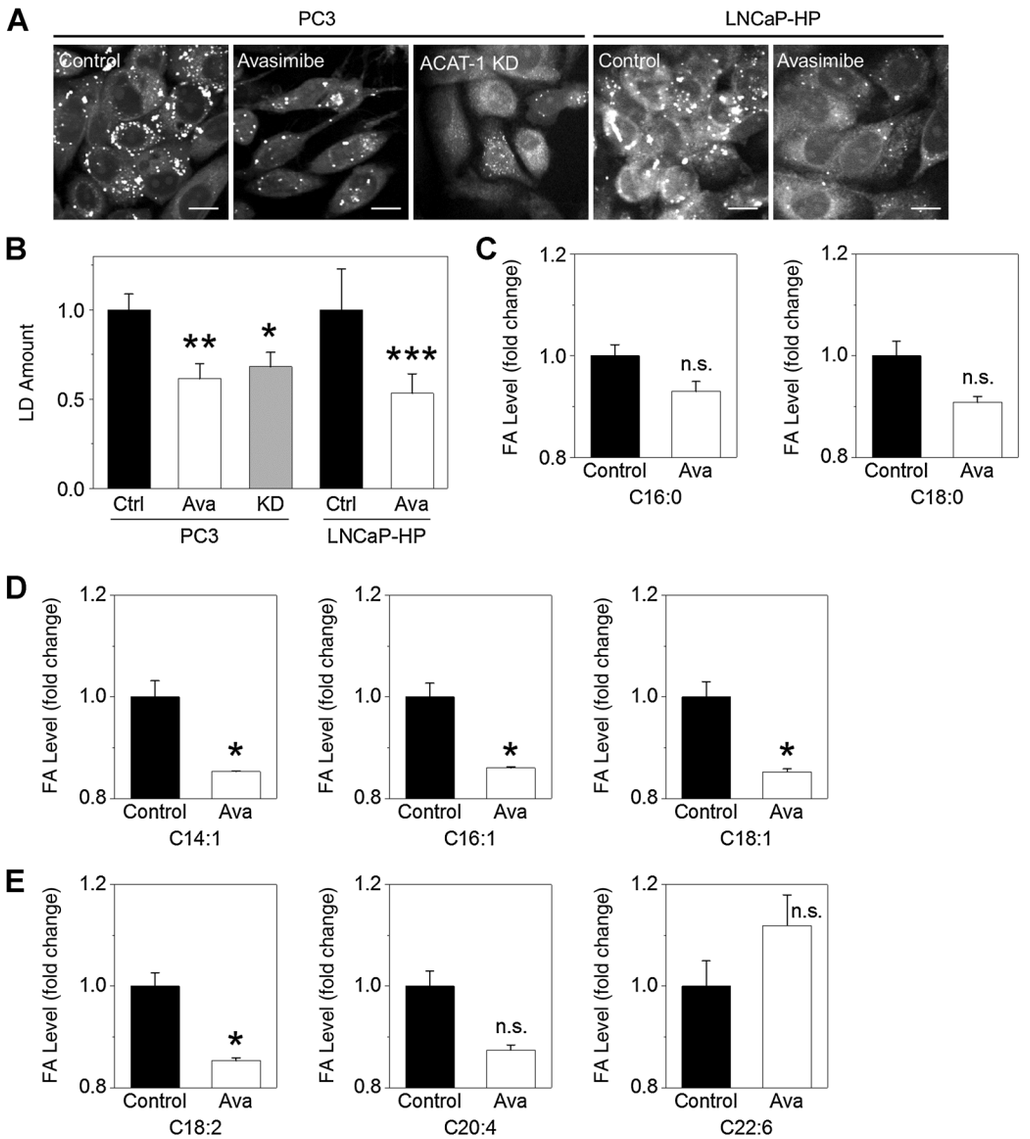

Figure 5.

ACAT inhibition reduces fatty acid levels in prostate cancer. **A,** SRS images of PC-3 and LNCaP-HP cells treated with avasimibe (10 μmol/L, 2 days) or with ACAT-1 shRNA. Scale bar, 10 μm. **B,** Quantitation of lipid droplet amount normalized to control groups. Error bars, SD ($n > 9$). **C–E,** LC-MS measurement of fatty acids from lipids extracted from PC-3. Fatty acid levels were normalized by cell number in each group. Fatty acids are grouped in saturated fatty acids (**C**), monounsaturated fatty acids (**D**), and polyunsaturated fatty acids (**E**). Error bars, SEM ($n = 3$). *, $P < 0.05$; **, $P < 0.005$; n.s., not significant; LD, lipid droplet.

cancer prostate cancer cells is esterified and stored in lipid droplets by ACAT, and high level of lipid synthesis and/or uptake (42, 43) provides sustained, ample supply of fatty acids (i.e., palmitic acid and palmitoleic acid) for acylation of Wnt protein. Lipid-modified Wnt is secreted and bound to membrane to exert its functions, such as promoting cell migration and invasion. By inhibition of cholesterol esterification, expression and cleavage of Sterol Regulatory Element-binding Protein-1 (SREBP-1) decreased as we reported previously (19). Consequently, the unavailability of fatty acids inhibited the Wnt acylation and secretion. Unable to bind to the membrane, the inactivation of Wnt/β-catenin signaling suppressed prostate cancer migration and metastasis.

Discussion

Metastatic prostate cancer is a deadly disease still in need of effective treatment. Androgen deprivation therapy (ADT) is the first-line hormone treatment for metastatic prostate cancer. Despite initial tumor regression, progression into castration-resistant prostate cancer is inevitable (21). Although drugs that target androgen receptor or androgen synthesis (i.e., enzalutamide or abiraterone) show clinical benefits, resistance to these treatments eventually occur (44). These phenomena show that current therapeutic strategies for metastatic prostate cancer are still not curative (21) and development of new treatments is needed to improve patient outcomes.

Published OnlineFirst March 15, 2018; DOI: 10.1158/1541-7786.MCR-17-0665

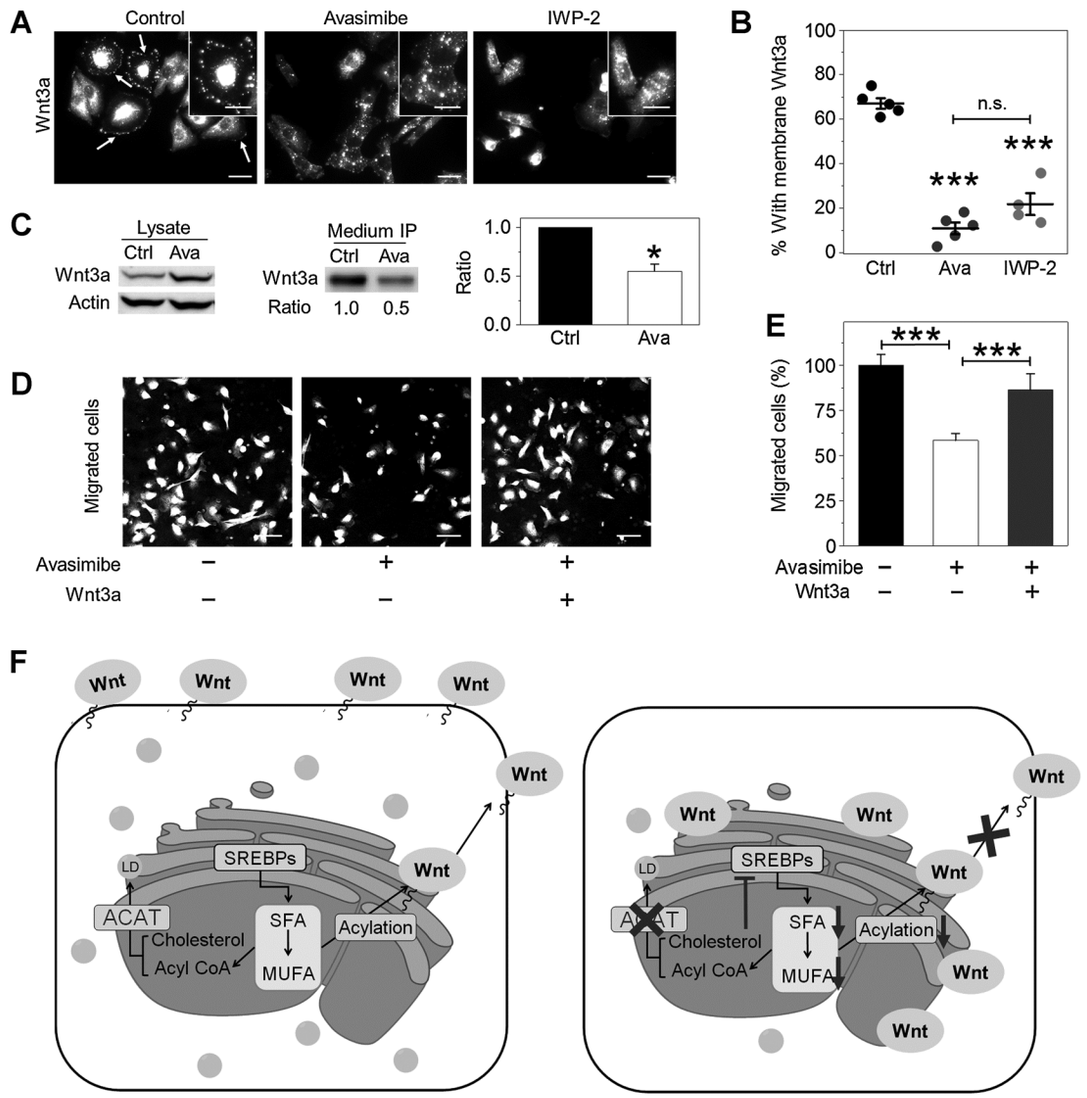

Figure 6.

CE depletion inhibits cell migration through reducing Wnt3a secretion. **A,** Immunofluorescence staining of Wnt3a in DU145 PTEN-KD treated with avasimibe (10 μmol/L, 2 days) or IWP-2 (10 μmol/L, 1 day). Arrows indicate membrane localized Wnt3a. Scale bar, 25 μm. Insert scale bar, 10 μm. **B,** Quantification of cells with membrane Wnt3a after avasimibe or IWP-2 treatment as indicated in **A**. **C,** Immunoblot of antibodies against Wnt3a and β-actin in DU145 PTEN-KD treated with avasimibe (10 μmol/L, 2 days). Medium Wnt3a was immunoprecipitated and normalized by precipitated protein concentration. Error bars, SD ($n = 3$). *, $P < 0.05$. **D,** Representative images of migration of cells pre-treated with avasimibe (10 μmol/L, 2 days) and subsequent Wnt3a supplement (100 ng/mL). Scale bar, 50 μm. **E,** Quantitation of migrated cells shown in **D**. Error bars, SD ($n = 3$). ***, $P < 0.0005$. **F,** Schematic showing the molecular mechanism. In metastatic prostate cancer, high level of lipid synthesis and/or uptake provides fatty acid substrates for Wnt acylation. This process is accompanied by conversion of excess cholesterol to CE by ACAT and stored in lipid droplets. Wnt acylation allows secretion and binding of Wnt to the membrane to drive cell migration and invasion. Suppressing cholesterol esterification by ACAT inhibition downregulates SREBP through negative feedback loop. As a result, lipogenesis pathway is suppressed, which limits the availability of free fatty acids required for Wnt acylation. Metastasis is then inhibited by reduced secretion of Wnt protein. SFA, saturated fatty acid; MUFA, unsaturated fatty acid; LD, lipid droplet.

In this study, we revealed an essential role of CE in metastasis and its potential as a therapeutic target for metastatic prostate cancer. Using two animal models that focus on different aspects of metastatic prostate cancer, we tested the therapeutic benefits of CE depletion on development of metastasis and growth of metastatic tumors in mice. Prostate cancer metastasis in an orthotopic mouse model involves escape of cancer cells from the primary tumor site and migration into other organs. It also provides information about the therapeutic effect on the primary tumor. Using this mouse model, we observed striking phenotypic differences between the primary tumors in vehicle versus that in avasimin-treated mice, which provides strong evidence that ACAT inhibition suppresses invasiveness of prostate cancer cells. Consistently, we observed a reduced number of metastatic nodules in avasimin-treated mice, supporting that ACAT inhibition suppresses development of metastasis during prostate cancer progression.

Published OnlineFirst March 15, 2018; DOI: 10.1158/1541-7786.MCR-17-0665

The intracardiac injection mouse model introduces the tumor cells directly into circulation, thus emphasizing the survival and growth of prostate cancer cells in other organs. Thus, we used this model to evaluate therapeutic efficacy of CE depletion in mice with metastatic prostate cancer already developed. Our results indicate that avasimin treatment effectively suppressed growth of metastatic prostate cancer in multiple organs. Importantly, we did not observe detectable toxicity from avasimin to the animals. This is because CE content is usually low in most normal cell types (1, 5), giving a unique opportunity to specifically target prostate cancer cells without causing unfavorable disturbance to the cholesterol homeostasis in most of normal cells. Indeed, there is an increasing body of evidence showing accumulation of CE in various types of cancer, including prostate cancer (19), breast cancer (45), leukemia (46), glioblastoma (47), and pancreatic cancer (48). These studies collectively support the importance of the cholesterol storage pathway in malignancy.

We observed reduced free monounsaturated fatty acid levels after ACAT inhibition. We suspect that as a consequence of inhibiting cholesterol esterification, free cholesterol level is increased, which downregulates SREBP activities through sterol-dependent negative feedback loop (6). This is supported by our previous finding that expression and cleavage of SREBP-1c are reduced upon CE depletion (19). As SREBP-1c is the isoform that mainly promotes fatty acid biosynthetic pathway (49), our observation of decreased fatty acid levels after inhibiting cholesterol esterification is likely to be through the regulation of SREBP-1c. Importantly, it has been reported that depleting SREBP results in reduction in the monounsaturated fatty acids in the cellular pool of free fatty acids (50), which supports our hypothesis. As the enzyme catalyzing the rate-limiting step in unsaturated fatty acid synthesis, SCD1, is directly regulated by SREBP-1c (51), it is possible that the level of monounsaturated fatty acids is reduced by downregulation of SCD1. Overall, given that SREBP-1 has been proposed to be an important regulator that provides a link between oncogenic signaling and tumor metabolism (50, 52), we believe that SREBP-1 plays an essential role in lipid homeostasis in during prostate cancer progression.

Finally, our results reveal that lipid metabolism is an important regulator of Wnt activity. Several studies show that Wnt acylation by acyltransferase Porcupine is essential for its secretion and binding to membrane receptors (41, 53). In a recent study, alterations in the Wnt signaling pathway were observed in 18% of patients with metastatic castration-resistant prostate cancer (54). Interestingly, it was reported that patients with alterations in these genes are predicted to respond to Porcupine inhibitors, such as IWP-2 (53), which supports the importance of Wnt acylation in prostate cancer progression. During acylation, a sufficient fatty acid pool is as critical as the expression of involved proteins. In support of this concept, overexpression of fatty acid synthase was shown to promote palmitoylation of Wnt protein in human prostate epithelial cells (55). In our study, we show that palmitoleic acid level regulates Wnt secretion in prostate cancer, which is essential for cell migration (Figs. 5 and 6). Collectively, these results show an important crosstalk between lipid metabolism and Wnt signaling, which work cooperatively to promote prostate cancer metastasis.

Disclosure of Potential Conflicts of Interest

No potential conflicts of interest were disclosed.

Authors' Contributions

Conception and design: H.J. Lee, J. Li, R.E. Vickman, B.D. Elzey, X. Liu, J.-X. Cheng

Development of methodology: H.J. Lee, J. Li, B.D. Elzey, J.-X. Cheng

Acquisition of data (provided animals, acquired and managed patients, provided facilities, etc.): H.J. Lee, J. Li, R.E. Vickman, R. Liu, A. Durkes, B.D. Elzey, T.L. Ratliff

Analysis and interpretation of data (e.g., statistical analysis, biostatistics, computational analysis): H.J. Lee, J. Li, R.E. Vickman, R. Liu, A. Durkes, B.D. Elzey, T.L. Ratliff, J.-X. Cheng

Writing, review, and/or revision of the manuscript: H.J. Lee, A. Durkes, B.D. Elzey, S. Yue, T.L. Ratliff, J.-X. Cheng

Administrative, technical, or material support (i.e., reporting or organizing data, constructing databases): H.J. Lee, X. Liu, J.-X. Cheng

Study supervision: X. Liu, T.L. Ratliff, J.-X. Cheng

Acknowledgments

This work was supported by a Department of Defense grant W81XWH-14-1-0557 (to J.-X. Cheng, X. Liu, and T. L. Ratliff). The authors acknowledge the support from the Purdue University Center for Cancer Research, NIH grant P30 CA023168 (to T. L. Ratliff). S. Yue acknowledges the support from National Natural Science Foundation of China 81501516.

The authors greatly appreciate the help from Scott A. Crist and Kinam Park for their insightful comments; Sandra Torregrosa-Allen, Melanie Currie, Puting Dong, and Janelle W. Salameh for their expert help in the animal experiments; Gabrielle Shafer and Meaghan M. Broman for their expert help in the histology; Amber H. Jannasch for her expert help in the mass spectrometry experiments;Clara Suh, Yifan Kong, Ruixin Wang, Paula Cooper, and Yimin Huang for their expert help in the cell experiments.

The costs of publication of this article were defrayed in part by the payment of page charges. This article must therefore be hereby marked *advertisement* in accordance with 18 U.S.C. Section 1734 solely to indicate this fact.

Received November 13, 2017; revised January 11, 2018; accepted February 22, 2018; published first March 15, 2018.

References

1. Chang TY, Chang CC, Ohgami N, Yamauchi Y. Cholesterol sensing, trafficking, and esterification. Annu Rev Cell Dev Biol 2006; 22:129–57.
2. Ikonen E. Cellular cholesterol trafficking and compartmentalization. Nat Rev Mol Cell Biol 2008;9:125–38.
3. Mann RK, Beachy PA. Novel lipid modifications of secreted protein signals. Annu Rev Biochem 2004;73:891–923.
4. Phillips MC. Molecular mechanisms of cellular cholesterol efflux. J Biol Chem 2014;289:24020–9.
5. Chang TY, Li BL, Chang CC, Urano Y. Acyl-coenzyme A:cholesterol acyltransferases. Am J Physiol Endocrinol Metab 2009;297: E1–9.
6. Goldstein JL, DeBose-Boyd RA, Brown MS. Protein sensors for membrane sterols. Cell 2006;124:35–46.
7. Kuzu OF, Noory MA, Robertson GP. The role of cholesterol in cancer. Cancer Res 2016;76:2063.
8. Freed-Pastor WA, Mizuno H, Zhao X, Langerod A, Moon SH, Rodriguez-Barrueco R, et al. Mutant p53 disrupts mammary tissue architecture via the mevalonate pathway. Cell 2012;148:244–58.
9. Sorrentino G, Ruggeri N, Specchia V, Cordenonsi M, Mano M, Dupont S, et al. Metabolic control of YAP and TAZ by the mevalonate pathway. Nat Cell Biol 2014;16:357–66.
10. Swyer GIM. The cholesterol content of normal and enlarged prostates. Cancer Res 1942;2:372–5.

Published OnlineFirst March 15, 2018; DOI: 10.1158/1541-7786.MCR-17-0665

11. Krycer JR, Brown AJ. Cholesterol accumulation in prostate cancer: a classic observation from a modern perspective. Biochim Biophys Acta 2013;1835: 219–29.
12. Locke JA, Guns ES, Lubik AA, Adomat HH, Hendy SC, Wood CA, et al. Androgen levels increase by intratumoral de novo steroidogenesis during progression of castration-resistant prostate cancer. Cancer Res 2008;68: 6407–15.
13. Leon CG, Locke JA, Adomat HH, Etinger SL, Twiddy AL, Neumann RD, et al. Alterations in cholesterol regulation contribute to the production of intratumoral androgens during progression to castration-resistant prostate cancer in a mouse xenograft model. Prostate 2010;70:390–400.
14. Zhuang L, Kim J, Adam RM, Solomon KR, Freeman MR. Cholesterol targeting alters lipid raft composition and cell survival in prostate cancer cells and xenografts. J Clin Invest 2005;115:959–68.
15. Freeman MR, Cinar B, Kim J, Mukhopadhyay NK, Di Vizio D, Adam RM, et al. Transit of hormonal and EGF receptor-dependent signals through cholesterol-rich membranes. Steroids 2007;72:210–17.
16. Adam RM, Mukhopadhyay NK, Kim J, Di Vizio D, Cinar B, Boucher K, et al. Cholesterol sensitivity of endogenous and myristoylated Akt. Cancer Res 2007;67:6238–46.
17. Dong P, Flores J, Pelton K, Solomon KR. Prohibitin is a cholesterol-sensitive regulator of cell cycle transit. J Cell Biochem 2010;111:1367–74.
18. Fukuchi J, Hiipakka RA, Kokontis JM, Hsu S, Ko AL, Fitzgerald ML, et al. Androgenic suppression of ATP-binding cassette transporter A1 expression in LNCaP human prostate cancer cells. Cancer Res 2004;64:7682–5.
19. Yue S, Li J, Lee SY, Lee HJ, Shao T, Song B, et al. Cholesteryl ester accumulation induced by PTEN loss and PI3K/AKT activation underlies human prostate cancer aggressiveness. Cell Metab 2014;19:393–406.
20. Siegel RL, Miller KD, Jemal A. Cancer statistics, 2017. CA Cancer J Clin 2017;67:7–30.
21. Watson PA, Arora VK, Sawyers CL. Emerging mechanisms of resistance to androgen receptor inhibitors in prostate cancer. Nat Rev Cancer 2015; 15:701–1.
22. Igawa T, Lin FF, Lee MS, Karan D, Batra SK, Lin MF. Establishment and characterization of androgen-independent human prostate cancer LNCaP cell model. The Prostate 2002;50:222–35.
23. Unni E, Sun S, Nan B, McPhaul MJ, Cheskis B, Mancini MA, et al. Changes in androgen receptor nongenotropic signaling correlate with transition of LNCaP cells to androgen independence. Cancer Res 2004;64:7156–68.
24. Zhang D, Slipchenko MN, Cheng JX. Highly sensitive vibrational imaging by femtosecond pulse stimulated Raman loss. J Phys Chem Lett 2011;2: 1248–53.
25. Slipchenko MN, Le TT, Chen H, Cheng JX. High-speed vibrational imaging and spectral analysis of lipid bodies by compound Raman microscopy. J Phys Chem B 2009;113:7681–86.
26. Lee SS, Li J, Tai JN, Ratliff TL, Park K, Cheng JX. Avasimibe encapsulated in human serum albumin blocks cholesterol esterification for selective cancer treatment. ACS Nano 2015;9:2420–32.
27. Park SI, Kim SJ, McCauley LK, Gallick GE. Pre-clinical mouse models of human prostate cancer and their utility in drug discovery. Curr Protoc Pharmacol 2010;Chapter 14:Unit14.15.
28. Pavese J, Ogden IM, Bergan RC. An orthotopic murine model of human prostate cancer metastasis. J Vis Exp 2013:e50873.
29. Yang WC, Adamec J, Regnier FE. Enhancement of the LC/MS analysis of fatty acids through derivatization and stable isotope coding. Anal Chem 2007;79:5150–7.
30. Movasaghi Z, Rehman S, Rehman IU. Raman spectroscopy of biological tissues. Appl Spectrosc Rev 2007;42:493–541.
31. Kozlowski JM, Fidler IJ, Campbell D, Xu ZL, Kaighn ME, Hart IR. Metastatic behavior of human tumor cell lines grown in the nude mouse. Cancer Res 1984;44:3522–9.
32. Edamura K, Nasu Y, Takaishi M, Kobayashi T, Abarzua F, Sakaguchi M, et al. Adenovirus-mediated REIC/Dkk-3 gene transfer inhibits tumor growth and metastasis in an orthotopic prostate cancer model. Cancer Gene Ther 2007;14:765–72.
33. Tripathi V, Popescu NC, Zimonjic DB. DLC1 induces expression of E-cadherin in prostate cancer cells through Rho pathway and suppresses invasion. Oncogene 2014;33:724–33.
34. Zhang H, Pan Y, Zheng L, Choe C, Lindgren B, Jensen ED, et al. FOXO1 inhibits Runx2 transcriptional activity and prostate cancer cell migration and invasion. Cancer Res 2011;71:3257–67.
35. Chandran UR, Ma C, Dhir R, Bisceglia M, Lyons-Weiler M, Liang W, et al. Gene expression profiles of prostate cancer reveal involvement of multiple molecular pathways in the metastatic process. BMC Cancer 2007;7:64.
36. Yu YP, Yu G, Tseng G, Cieply K, Nelson J, Defrances M, et al. Glutathione peroxidase 3, deleted or methylated in prostate cancer, suppresses prostate cancer growth and metastasis. Cancer Res 2007;67:8043–50.
37. Bowen C, Bubendorf L, Voeller HJ, Slack R, Willi N, Sauter G, et al. Loss of NKX3.1 expression in human prostate cancers correlates with tumor progression. Cancer Res 2000;60:6111–5.
38. Kypta RM, Waxman J. Wnt/beta-catenin signalling in prostate cancer. Nat Rev Urol 2012;9:418–28.
39. Dubrovska A, Kim S, Salamone RJ, Walker JR, Maira SM, Garcia-Echeverria C, et al. The role of PTEN/Akt/PI3K signaling in the maintenance and viability of prostate cancer stem-like cell populations. Proc Natl Acad Sci U S A 2009;106:268–73.
40. Willert K, Brown JD, Danenberg E, Duncan AW, Weissman IL, Reya T, et al. Wnt proteins are lipid-modified and can act as stem cell growth factors. Nature 2003;423:448–52.
41. Takada R, Satomi Y, Kurata T, Ueno N, Norioka S, Kondoh H, et al. Monounsaturated fatty acid modification of Wnt protein: its role in Wnt secretion. Dev Cell 2006;11:791–801.
42. Migita T, Ruiz S, Fornari A, Fiorentino M, Priolo C, Zadra G, et al. Fatty acid synthase: a metabolic enzyme and candidate oncogene in prostate cancer. J Natl Cancer Inst 2009;101:519–32.
43. Wu X, Daniels G, Lee P, Monaco ME. Lipid metabolism in prostate cancer. Am J Clin Exp Urol 2014;2:111–20.
44. Ferraldeschi R, Welti J, Luo J, Attard G, de Bono JS. Targeting the androgen receptor pathway in castration-resistant prostate cancer: progresses and prospects. Oncogene 2015;34:1745–57.
45. de Gonzalo-Calvo D, Lopez-Vilaro L, Nasarre L, Perez-Olabarria M, Vazquez T, Escuin D, et al. Intratumor cholesteryl ester accumulation is associated with human breast cancer proliferation and aggressive potential: a molecular and clinicopathological study. BMC Cancer 2015;15:460.
46. Mulas MF, Abete C, Pulisci D, Pani A, Massidda B, Dessi S, et al. Cholesterol esters as growth regulators of lymphocytic leukaemia cells. Cell Prolif 2011;44:360–371.
47. Geng F, Cheng X, Wu X, Yoo JY, Cheng C, Guo JY, et al. Inhibition of SOAT1 suppresses glioblastoma growth via blocking SREBP-1-mediated lipogenesis. Clin Cancer Res 2016;22:5337–48.
48. Li J, Gu D, Lee SS, Song B, Bandyopadhyay S, Chen S, et al. Abrogating cholesterol esterification suppresses growth and metastasis of pancreatic cancer. Oncogene 2016;35:6378–88.
49. Amemiya-Kudo M, Shimano H, Hasty AH, Yahagi N, Yoshikawa T, Matsuzaka T, et al. Transcriptional activities of nuclear SREBP-1a, -1c, and -2 to different target promoters of lipogenic and cholesterogenic genes. J Lipid Res 2002;43:1220–35.
50. Griffiths B, Lewis CA, Bensaad K, Ros S, Zhang Q, Ferber EC, et al. Sterol regulatory element binding protein-dependent regulation of lipid synthesis supports cell survival and tumor growth. Cancer Metab 2013;1:3.
51. Tabor DE, Kim JB, Spiegelman BM, Edwards PA. Identification of conserved cis-elements and transcription factors required for sterol-regulated transcription of stearoyl-CoA desaturase 1 and 2. J Biol Chem 1999;274: 20603–10.
52. Guo D, Bell EH, Mischel P, Chakravarti A. Targeting SREBP-1-driven lipid metabolism to treat cancer. Curr Pharm Des 2014;20:2619–26.
53. Liu J, Pan S, Hsieh MH, Ng N, Sun F, Wang T, et al. Targeting Wnt-driven cancer through the inhibition of Porcupine by LGK974. Proc Natl Acad Sci U S A 2013;110:20224–9.
54. Dan R, Van Allen EM, Wu YM, Schultz N, Lonigro RJ, Mosquera JM, et al. Integrative clinical genomics of advanced prostate cancer. Cell 2015;161: 1215–28.
55. Fiorentino M, Zadra G, Palescandolo E, Fedele G, Bailey D, Fiore C, et al. Overexpression of fatty acid synthase is associated with palmitoylation of Wnt1 and cytoplasmic stabilization of beta-catenin in prostate cancer. Lab Invest 2008;88:1340–8.

Published OnlineFirst March 15, 2018; DOI: 10.1158/1541-7786.MCR-17-0665

Molecular Cancer Research

Cholesterol Esterification Inhibition Suppresses Prostate Cancer Metastasis by Impairing the Wnt/ β-catenin Pathway

Hyeon Jeong Lee, Jie Li, Renee E. Vickman, et al.

Mol Cancer Res 2018;16:974-985. Published OnlineFirst March 15, 2018.